Zhou *et al. Journal of Nanobiotechnology* (2025) 23:238
https://doi.org/10.1186/s12951-025-03147-x

Journal of Nanobiotechnology

RESEARCH Open Access

DNAzyme hydrogels specifically inhibit the NLRP3 pathway to prevent radiation-induced skin injury in mice

Daijun Zhou[1], Zhihui Li[1†], Linbo Bao[1†], Xiang Zhao[2], Jie Hao[2], Chuan Xu[1], Feifan Sun[1], Dan He[3], Chaoyang Jiang[1*], Tian Zeng[2*] and Dong Li[1*]

Abstract

Radiation-induced skin injury (RISI) is a frequent complication of radiotherapy, yet current preventive strategies exhibit suboptimal efficacy. Our previous publications have consistently demonstrated the effectiveness of biomaterials and hydrogels in preventing RISI. Based on comprehensive literature reviews, we speculate that NLRP3 overexpression plays a central role in the development of RISI. Therefore, designing DNAzyme (DZ)-hydrogels with targeted inhibition of NLRP3 overexpression is crucial for preventing RISI.To achieve this, we designed and screened the optimal NLRP3-DZ using bioinformatics, molecular dynamics, and gel electrophoresis methods. We encapsulated the NLRP3-DZ within ZIF-8 to enhance its stability, controlled release, and safety. To enhance the material's transdermal penetration and practicality, we attached the TAT transmembrane peptide. The final preparation and characterization of NLRP3-DZ@ZIF-8/TAT was achieved.In vitro cell models revealed that DZ-hydrogels exhibit high biosafety, effectively inhibit NLRP3 expression, promote cell migration, inhibit cell apoptosis, and possess antibacterial properties. Genomics analysis suggested that DZ-hydrogels may exert these functions by regulating changes in relevant mRNA pathways.Furthermore, we established a mouse model of RISI and found that the material can promote wound healing by regulating proteins associated with apoptosis, oxidative stress, and the inflammatory response. These research findings provide valuable insights for the prevention of RISI using DZ-hydrogels.

Keywords Radiation-induced skin injury, NLRP3, DNAzyme, Hydrogels

†Zhihui Li and Linbo Bao co-first author.

The corresponding author is Dong Li and the co-corresponding authors are Tian Zeng and Chaoyang Jiang.

*Correspondence:
Chaoyang Jiang
bvsid125@163.com
Tian Zeng
zengtian@tmmu.edu.cn
Dong Li
Dongli81cd@qq.com
[1]Department of Oncology, General Hospital of Western Theater Command, Chengdu 610083, China
[2]Department of Oncology, Southwest Hospital, Army Medical University, Chongqing 400038, China
[3]Department of Oncology, The Second Affiliated Hospital of Chengdu Medical College, National Nuclear Corporation 416 Hospital, Chengdu 610051, China

Introduction

The skin is the primary organ exposed to ionizing radiation, especially during radiotherapy, and it exhibits high sensitivity to radiation. Typically, skin absorption of a radiation dose exceeding 20–30 Gy can lead to the development of ulcers. Radiation-Induced Skin Injury (RISI) is closely associated with exposure to one or multiple high doses of radiation [1]. Compared to other types of skin injuries, RISI displays unique phases characterized by latency, expansiveness, and progression. In the initial stage, RISI typically presents as localized skin pain and itching. In severe cases, it may progress to ulcers, peeling, and local infection. With continued accumulation of radiation dose, RISI can potentially lead to necrosis of the skin tissue and, in some instances, even cancer [2]. According to statistics [3], the incidence of RISI in radiotherapy patients can exceed 80%, typically beginning 2–3 weeks after radiotherapy initiation with the highest cumulative radiation dose and most severe damage occurring towards the end of treatment. Pursuant to the RTOG toxicity criteria established by the American Radiation Oncology Collaboration Group[4], while RISI categorized as Grade 0-II does not directly compromise the efficacy of radiotherapy, it frequently detracts from patients' quality of life. Conversely, for cases of Grade III-IV RISI, the consideration of radiotherapy suspension arises, ultimately risking unfettered tumor proliferation. This predicament poses a formidable challenge in clinical radiotherapy, necessitating prompt intervention. The current armamentarium of clinical interventions for RISI encompasses the topical application of triethanolamine cream (Biafen), local antibiotic administration, and therapy augmented by cell growth factors[5].

Ma et al. suggested that highly efficient prevention of radiation dermatitis using a PEGylated superoxide dismutase dissolving microneedle patch [6]. In 2022, our research ventured into combining graphene oxide (GO) with sodium alginate (SA) and interferon α-induced protein 6 (IFI6), mediated by polydopamine (PDA) adhesion, to create IFI6/SA/GO@PDA [7]. This innovative formulation revolves around a slow-release mechanism for IFI6, fostering the proliferation of irradiated epidermal cells (HaCaT), while mitigating apoptosis and reactive oxygen species (ROS) generation, thus safeguarding the irradiated skin cells. Further advancing our efforts, another study in 2022 integrated miRNA into our intervention strategy [8], Specifically, miR181a was encapsulated within an erythrocyte membrane (EM) containing hemoglobin (HB), with IFI6 externally attached, resulting in the synthesis of IFI6/miR181a/@EM-HB. This composite system effectively delivers miR181a to augment DNA damage repair in post-irradiated skin cells, demonstrating a potent synergistic action alongside IFI6 in thwarting radiation dermatitis in mice.Huang et al. also design that immunomodulatory hydrogel patches loaded with curcumin and tannic acid assembled nanoparticles for radiation dermatitis repair and radioprotection [9]. In addition, there are studies used exploring black soybean extract cream for inflammatory dermatitis—toward radiation dermatitis relief [10]. While these studies underscore the promise of biomaterials in RISI prevention, they were not exclusively tailored to address the underlying core mechanisms of RISI.

Revisiting the foundational mechanisms of RISI from a cellular biology viewpoint [2, 11, 12], it is evident that the primary manifestation stems from radiation-triggered overproduction of reactive oxygen species (ROS), which subsequently orchestrates cellular apoptosis. Delving into the realm of molecular biology, the core lies in the ignition of the NLRP3 (NOD-like receptor thermal protein domain associated protein 3) inflammasome and other integral innate immune pathways, ultimately precipitating a cascade of inflammatory reactions. The underlying radiation-induced damage in RISI is predominantly attributable to oxidative stress fueled by ROS. This, in turn, activates NF-κB signaling pathways and prompts early response transcription factors, initiating diverse signal cascades such as NADPH oxidase, cyclooxygenase-2 (COX-2), and nitric oxide synthase (iNOS) [13]. Furthermore, both ROS and the inflammatory responses perpetuate mitochondrial dysfunction and apoptosis, concurrently activating the NLRP3 inflammasome pathway. The activation of this inflammasome propels caspase-1 activation, culminating in the release of proinflammatory cytokines IL-18 and IL-1β [14]. Collectively, these findings underscore the pivotal role of radiation-induced ROS activation in facilitating RISI progression via the NLRP3 inflammasome.It is noteworthy that, despite the numerous mechanistic advantages of NLRP3 for the treatment of radiation-induced skin injuries, it suffers from poor skin penetration and the nucleic acid molecules are prone to degradation due to their instability, which are issues that also need to be addressed [15]. As a unique branch of DNA-based materials, DNA hydrogels have exhibited many fascinating characteristics, including broad biocompatibility, precise programmability, convenient modification, and tunable mechanical properties, which make DNA hydrogels ideal biomaterials [16]. Moreover, by combining with functional nucleic acids, such as aptamers, i-motif nanostructures, CpG oligodeoxynucleotides, and DNAzymes, DNA hydrogels can be further tailored to provide additional target recognition, therapeutic potential, and catalytic activities, allowing them to play important roles in biosensing and medical applications [16, 17]. Therefore, the design of drug delivery system for NLRP3-DZ hydrogel in this study aims to be realized by combining ZIF-8 and Trans-activator of Transcription (TAT).

ZIF-8 nanoparticles have emerged as multifunctional nanocarriers, offering a promising alternative.ZIF-8 nanoparticles possess the capability to regulate functional nucleic acids, such as DNAzymes and miRNAs, through electrostatic and ligand interactions. This feature enables ZIF-8 to effectively accumulate targeted nucleic acids, thereby enhancing their permeability and retention effects within the desired tissue. Importantly, ZIF-8 facilitates the uptake of nucleic acids, ensuring their stability and prevention from cellular degradation [15]. In the context of wound healing, the local acidic microenvironment plays a crucial role. ZIF-8 nanoparticles exploit this microenvironment by eliminating the coordination interaction between Zn^{2+} and imidazole, leading to the controlled release of nucleic acids at the wound site. This controlled release mechanism is particularly beneficial for wound healing applications, ensuring that the therapeutic agents are delivered precisely when and where they are needed [18]. Moreover, ZIF-8 nanoparticles are attractive vectors for genetic engineering due to their exceptional biodegradability and low cytotoxicity. Their biocompatible nature ensures that they can be safely used in various biomedical applications, including wound healing and drug delivery [19]. In summary, ZIF-8 nanoparticles represent a versatile and promising platform for transdermal delivery of solid nanomaterials. Their ability to regulate functional nucleic acids, promote controlled release in acidic microenvironments, and possess favorable biocompatibility underscores their potential in addressing the current challenges associated with transdermal delivery.

The TAT peptide exhibits remarkable cell-penetrating capabilities, allowing it to traverse the plasma and nuclear membranes of diverse living cells with ease [20]. Its potential extends beyond these barriers, as TAT can facilitate internalization via unsaturated pathways and mechanisms independent of receptors or transporters. This unique attribute enables TAT to readily cross the blood-brain barrier, biofilm barrier, and dense tumor tissue, thereby enhancing its therapeutic potential in various applications.Furthermore, TAT has been employed in fusion strategies to enhance the functionality of other polypeptides. For instance, studies have fused TAT with BORIS (Brother of Regulator of Imprinted Sites) polypeptide, resulting in the creation of BTApep-TAT, which demonstrates enhanced cell membrane penetration abilities [21]. This modification not only improves the stability and persistence of polypeptides in circulation but also underscores the versatility of TAT in drug delivery systems.Moreover, the synergistic effects of TAT when combined with other targeting moieties, such as Ang, have been investigated. The resulting extracellular vesicles, modified with this dipeptide combination, harness the efficient membrane penetration of TAT and the glioma-targeting capabilities of Ang, while also mitigating the issue of Ang receptor saturation [21, 22]. These advancements illustrate how TAT-modified materials are emerging as innovative solutions in the field of drug bioutilization.In summary, the TAT peptide's ability to traverse biological barriers, enhance the stability and functionality of fused polypeptides, and facilitate targeted delivery through synergistic interactions underscores its significance in drug development and delivery systems.

Therefore, we believe that synthesizing nanocomposites with high stability and sustainable enzymatic properties can be achieved by loading a substantial quantity of TAT transmembrane peptides and NLRP3-DZ onto ZIF-8. Furthermore, we have elucidated the intricate relationship between the NLRP3-DZ@ZIF-8/TAT material and the ROS/NLRP3 pathway, offering valuable insights into the underlying mechanisms of RISI. This study possesses considerable innovative and practical value.

Methodology

Ethics disclaimer

The Department of Oncology at Southwest Hospital supplied the cell cultures, whereas the male BALB/c mice (each weighing 25 g) were obtained from the Experimental Animal Department of Army Medical University. The mice were housed in an environment maintained at a temperature of 25℃ and a relative humidity of 50%, with each mouse being individually fed in accordance with a 12-hour circadian rhythm. The Animal Ethics Committee of Southwest Hospital approved all animal assays(AMUWEC20226175), and all work was conducted in accordance with relevant ethical regulations.

Sources of materials and reagents

NLRP3-DZ was purchased from Sangon Biotech (Shanghai, China), while ZIF-8 and TAT-related materials were obtained from Nanjing XFNANO Materials Tech Co., LTD. (Nanjing, China). The reagents used in biological experiments and material characterization assays were sourced from Shanghai Yansu Technology Co., LTD, Chengdu Guoao Technology Co., LTD, and Sichuan Anlai Biotechnology Co., LTD.

Relatively stable NLRP3-DZ sequence

We did this by retrieving the full-length mRNA sequence of mice and human NLRP3.Definition NLR family, pyrin domain containing 3(NLRP3),transcript variant 1, mRNA.Core coding region information and transcriptional protein sequence.

In view of the corresponding target sequence, using 10–23 deoxyuridine enzyme catalytic core, combining software analysis, to determine the secondary structure is less, and combination of substrate and relatively stable

NLRP3-for DNAzyme sequence.The nucleic acid drug product NLRP3-DNAzyme was synthesized by Sangon Biotech and purified by HPLC.

Preparation of NLRP3-DZ@ZIF-8/TAT

1) NLRP3-DZ@ZIF-8: 11 g zinc acetate, 1 mg NLRP3-DZ dissolved in 500 ml Tris solution(solution A). 0.65 g dimethylimidazole dissolved in 500 ml Tris solution is (solution B). Solution A and solution B were mixed under agitation and stirred for 2 h, and then centrifuged with methanol for 3 times, and precipitated and lyophilized into a white powder known as NLRP3-DZ@ZIF-8.
2) NLRP3-DZ@ZIF-8/TAT: The NLRP3-DZ@ZIF-8 obtained in the first step and 25 mg polypeptide were dispersed in 1000 ml Tris solvent, stirred away from light for 24 h, and then centrifuged with methanol for 3 times to precipitate and lyze-dry into white powder NLRP3-DZ@ZIF-8/TAT.

Characterization of NLRP3-DZ@ZIF-8/TAT

The characterization of NLRP3-DZ@ZIF-8/TAT was performed using scanning electron microscopy (SEM), transmission electron microscopy (TEM), and atomic force microscopy (AFM). The particle size and charge of the material were measured using a Zeta potential nanoparticle analyzer, while dynamic light scattering was employed to evaluate zeta potential and particle sizes. Fourier transform infrared (FTIR) spectra (4000–600 cm^{-1}) were recorded using a Nicolet 6700 FTIR spectrometer. Elemental composition analyses were performed using energy dispersive spectroscopy (EDS) and X-ray photoelectron spectroscopy (XPS), while crystal structures were assessed through an X-ray diffraction (XRD) approach.

NLRP3-DZ@ZIF-8/TAT-hydrogel viscosity (mPa·s) was measured at 21 ± 3 °C by DVE-RV Digital Viscometer, which involved the plotting of.selecting 2 min (time required for the viscosity reading to reach a constant value) as time of spindle rotation for each spindle rotational speed, namely 2.5, 5, 10, 20, 50 and 100 rpm.The calculation of % encapsulation efficiency (EE) and % drug loading (DL) was taken and then analyzed using a UV–vis spectrophotometer according to a derivatization method described with a visible wavelength.

The role of NLRP3-DZ@ZIF-8/TAT in cell models in vitro

Four distinct groups, labeled as Group A-D, were utilized for the cytological experiments. These groups consisted of normal cultures, normal cultures exposed to 3 Gy radiation, normal cultures exposed to 3 Gy radiation and treated with NLRP3-DZ, and normal cultures exposed to 3 Gy radiation and treated with NLRP3-DZ@ZIF-8/TAT, respectively.

1) Cell Biosafety: HaCat cultures (2×10^3 cells) were seeded into wells containing Group A-D. Cellular viability was assessed using CCK-8 assays after 1, 4, and 7 days of incubation.
2) Cell Staining: To investigate changes in cytoskeleton morphology, culture media for Group A-D a duration of 24 h. Following incubation, the stained cultures were imaged using confocal laser scanning microscopy (model 780, Zeiss™, Germany). Additionally, the HaCat cultures were subjected to DAPI and phalloidin staining, and the fluorescent intensities were subsequently quantified.
3) Cell Migration: HaCaT cells were permitted to grow to confluence prior to being plated onto 24 well plates at a density of 2×10^4 cells per well. A pipette tip was utilized to create a scratch across the monolayer at the 0-hour time point. After 12 h, the cultures were visualized using a Zeiss video microscope. This assay was conducted three times, with each cohort consisting of five replicates. Specific measurements were obtained using ImageJ® 1.48v software (NIH, USA).
4) Antibacterial Function Assessment: *E. coli*(strain numbers ATCC25922, seeded concentration 1×10^6 cfu·mL^{-1}) and *MRSA*(strain numbers ATCC33591, seeded concentration 1×10^6 cfu·mL^{-1}) supplied by the Army Medical University, were used for this study.Petri plates were then coated with equal amounts of these adjusted bacterial cultures and incubated for one day at 37 °C to assess changes in bacterial count.
5) Flow Cytometry Analysis: Cell apoptosis was studied using the Annexin V-FITC/PI Apoptotic Detection kit® (Dojindo Molecular Technologies™, Japan) in conjunction with flow cytometry. Cell evaluation was conducted using Cell Quest® software on a Fluorescence Activating Cell Sorter (FACS) instrument (Beckman Coulter™, USA).
6) Western Blot for NLRP3 Expression Detection: The NLRP3 Rabbit Monoclonal Antibody (Beyotime, China) was used at a 1:1000 dilution. Then collected and developed for chemiluminescence using reagents from Thermal Scientific™ (USA).

Gene and mRNA expression sequencing

The collection of total RNA was carried out using TRIzol® (TaKaRa Bio™, Japan), following the instructions provided in the kit. The integrity and purity of the RNA were assessed through 1% agarose gel electrophoresis to evaluate any breakdown or contamination. Sequencing libraries were prepared using the NEBNext®UltraTM

RNA Library Prep Kit for Illumina® (NEB, USA), and the library fragments were purified using the AMPure XP® system (Beckman Coulter™, USA) to select cDNA fragments of appropriate length for PCR. The products were further purified using the AMPure XP® system, and the quality of the libraries was evaluated using the Agilent™ Bioanalyzer 2100® platform. Sequencing was performed using the Illumina™ HiSeq 4000®, generating 150 bp paired-end reads.

We employed the GO (Gene Ontology, http://www.geneontology.org) and KEGG (Kyoto Encyclopedia of Genes and Genomes, http://www.genome.jp/kegg) databases for Annotation, Visualization, and Integrated Discovery(DAVID, https://david.ncifcrf.gov). KEGG enrichment analysis was used to determine intersecting gene pathways. Visualization of all resultant datasets was accomplished using ClusterProfiler®.

The role of NLRP3-DZ@ZIF-8/TAT in vivo mice models

Each mouse was anesthetized by administering approximately 0.2 ml of pentobarbital via intraperitoneal injection. Following this, a linear accelerator emitting 6 Mev electron rays was employed (with specifications including an irradiation field of 1 cm×1 cm, single irradiation at 30 Gy, duration of 10 min, and a dose rate of 300 cGy/min). In this setup, a distance of 1 m was maintained between the radiation source and the skin, and a lead plate was used to shield the remaining skin. Post-irradiation, the affected region of each cohort was coated with materials that were replaced at 48-hour intervals. This process spanned a total duration of 7–14 days, with the mice being divided into five cohorts, each consisting of five mice. Five different groups, referred to as Groups A-E, were used for the RISI experiments. These groups consisted of normal mice, normal mice + 30 Gy radiation, normal mice + 30 Gy radiation + NLRP3-DZ, normal mice + 30 Gy radiation + NLRP3-DZ@ZIF-8, and normal mice + 30 Gy radiation + NLRP3-DZ@ZIF-8/TAT, respectively.

To evaluate recovery activity, IPP6.0® conducted a comparative assessment of wound areas before and after recovery, utilizing the formula: Wound-recovery activity = [(initial wound area) − (wound area post-recovery at a fixed time)] / (initial wound area) × 100%.

Histopathology and immunofluorescence staining

1) Hematoxylin-Eosin Staining: Samples were collected 14 days later to prepare paraffinized sections. These sections were then stained using Hematoxylin-Eosin (HE). The length of the neoepithelium was measured by different pathology experts using a blinded approach.
2) Masson Staining: After Masson staining, muscle fibers appear red, while collagen fibers appear green or blue. This staining method is primarily used to distinguish collagen fibers from muscle fibers.
3) TUNEL and RT-PCR: TUNEL staining was primarily used to detect the breakage of nuclear DNA during apoptosis. The kit was labeled with FITC fluorescein, and the positive apoptotic nuclei appeared green. RT-PCR was mainly used to study changes in the expression levels of NLRP3 mRNA in the skin tissues of mice.

Statistical assessment

All table drawings and statistics-based datasets were generated using GraphPad Prism 9.0® software (GraphPad Software™, USA). Each assay was conducted on three separate occasions, with the dataset outcomes representing the mean ± standard error. All cell-based experiments were repeated at least 3 times, and each group in the mouse experiments included at least 6 mice.Pairwise comparisons between cohorts were conducted using one-way ANOVA, with a statistical significance threshold set at 5% ($P < 0.05$).

Results and discussion

Preparation and research flow diagram of NLRP3-DZ@ZIF-8/TAT hydrogels

The process of producing NLRP3-DZ@ZIF-8/TAT is illustrated in Fig. 1a. In recent years, the design and application of DNAzyme hydrogels for wound treatment have become a research hotspot. Zhu et al. designed and synthesized a G-quadruplex/hemin DNAzyme that functionalized AgNCs with G4/hemin [23], resulting in a silver-based dressing that exhibited potent therapeutic efficacy on infected wounds with excellent biosafety. Similarly, Mo et al. designed and synthesized a multienzyme-integrated DNAzyme nanocatalytic platform for efficient bacterial clearance and mitigation of inflammatory responses [24], making it adaptable to infected wounds.

As shown in Fig. 1b, drawing from the aforementioned conclusions, we posit that NLRP3-DZ can effectively suppress the activation of the NLRP3 inflammasome and counter the oxidative stress induced by ROS. The incorporation of TAT enhances the transdermal penetration and bioavailability of the material, while ZIF-8 amplifies the drug loading capacity, prolongs the action time, and enhances biosafety. The synergistic effect of the NLRP3-DZ@ZIF-8/TAT construct significantly accelerates wound healing in RISI, marking the first-ever application of anti-NLRP3 in the material science field. Lastly, an RISI model was established in mice (Fig. 1c), and the effects of NLRP3-DZ@ZIF-8/TAT on RISI wound

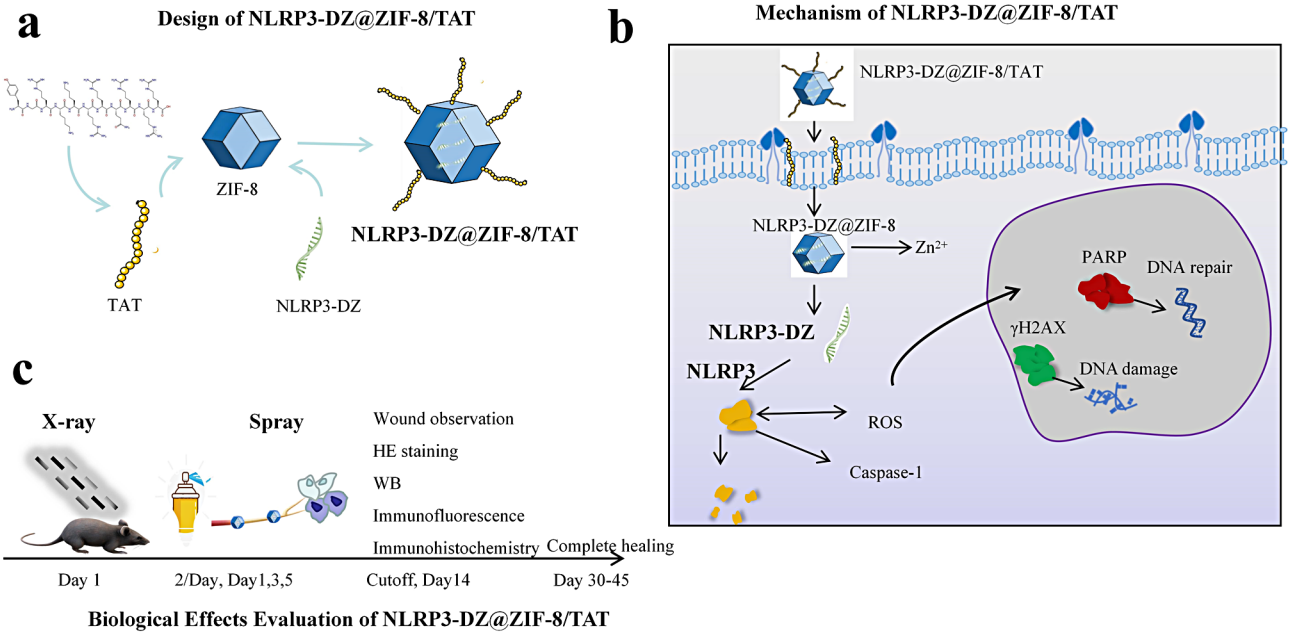

Fig. 1 NLRP3-DZ@ZIF-8/TAT Hydrogels Preparation and Research Flow Diagram. **a**: Hydrogels material design and preparation. **b**: Mechanism of NLRP3-DZ@ZIF-8/TAT. **c**: Biological effects evaluation of NLRP3-DZ@ZIF-8/TAT

recovery were assessed through observation and mechanistic studies.

Design and preparation of NLRP3-DZ

The 10–23 DNAzyme stands out as one of the most prominent catalytically active DNA sequences, with its ability to cleave a wide array of RNA targets with high selectivity, offering substantial therapeutic and biotechnological potential [24]. To explore this potential, we retrieved the full-length mRNA sequence of NLRP3. Borggrate et al. [25] propose that by employing a strategically chosen single-atom substitution, we can notably augment the performance of the DNAzyme. This underscores that the gained understanding of the molecular structure, its plasticity, and the presence of long-lived intermediate states serves as a valuable foundation for the rational design of next-generation DNAzymes.

We selected regions with few secondary structures, low free energy, and a rich cutting site base composition. In view of the corresponding target sequence, we used the 10–23 deoxyuridine enzyme catalytic core to determine regions with less secondary structure and a relatively stable NLRP3-DNAzyme sequence for GCAG ATCACAGGCTAGCTACAACGATCCTCAAAT(Mice) and TGAGGTCGGAGGCTAGCTACAACGATCCTC AAAC(Human). Molecular simulations of the NLRP3-DZ sequence were performed , including 2D simulations of NLRP3-DZ and the binding state of NLRP3-DZ and NLRP3-sub (Fig. 2a for mouse sequence and Fig. 2b for human sequence). The sequence difference between human and mouse is mainly reflected in the mutation of 5 bases, but the above difference is not obvious from the morphology of the simulated map. However, despite high expectations, DNAzymes have not yet been translated into clinical applications due to their low effectiveness in vivo. In the past five years, various aspects have been explored to optimize DNAzyme-integrated therapeutics, including structural stability, mechanism exploration, cell internalization rate, cofactor activation, and off-target effects [26]. DNA enzyme screening and verification are typically characterized by gel electrophoresis. Figure 2c shows that we verified through PAGE that the Dz designed can effectively cut NLRP3-sub in the presence of zinc ions, and can achieve 5 times the effective degradation of NLRP3-sub within 1 h. Similar to our study, Miao et al. report the successful completion of nine rounds of in vitro selection using an unmodified DNA library to identify specific DNAzymes of Vibrio cholerae [27]. The activity of these DNAzymes was assessed through fluorescence assay and gel electrophoresis.Meanwhile, Zhang et al. propose that by designing the toes of DNA nanotubes as G-quadruplexes, G-quadruplex arrays can be formed on pure DNA nanotubes, which subsequently bind to heme to create a nanotube-supported DNAzyme known as DNTzyme. Characterization of this DNAzyme was carried out using agarose gel electrophoresis, circular dichroism, and fluorescence microscopy [28]. Figure 2. Design and Preparation of NLRP3-DZ. a: Sequence structure characteristics and thermodynamic parameters of NLRP3-Dz, Structural characteristics and thermodynamic parameters of the combined products of NLRP3-Dz and substrate chains;

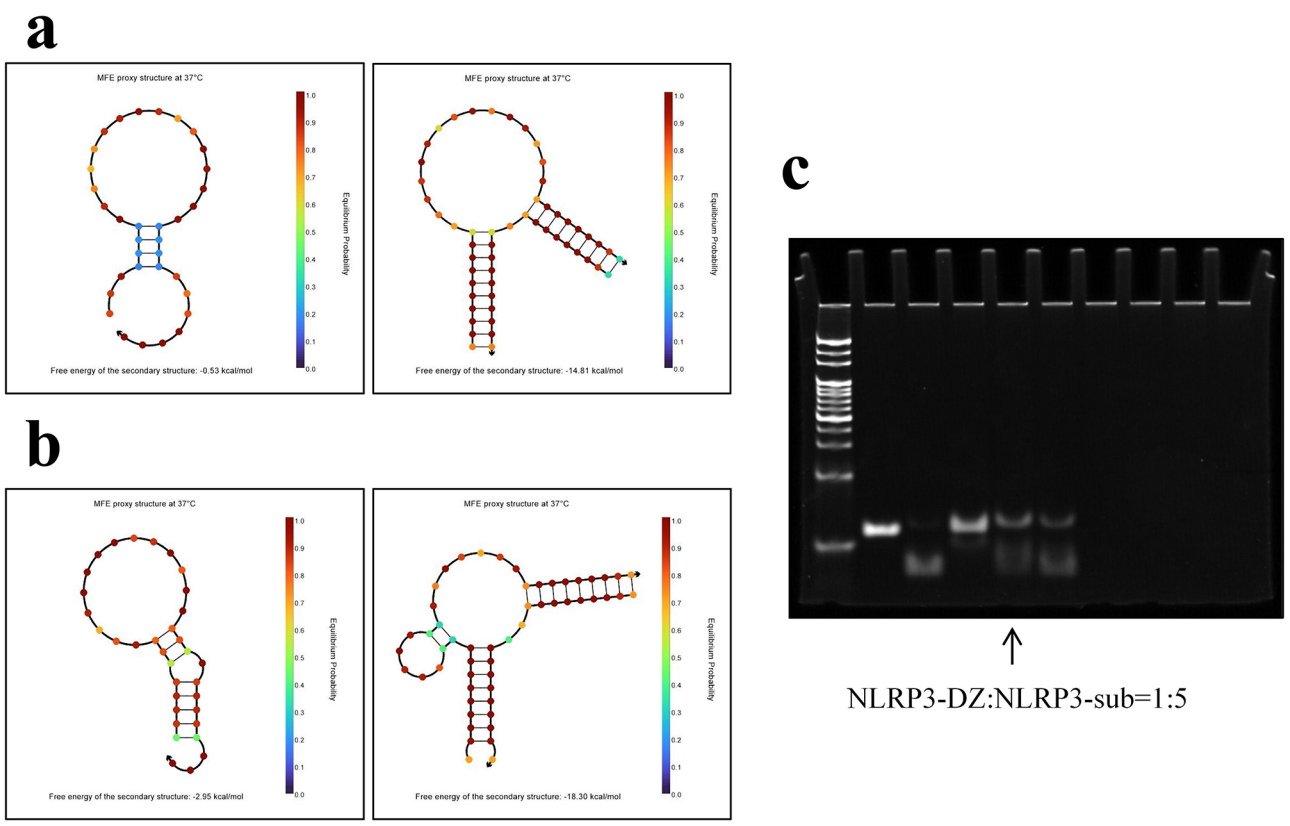

Fig. 2 Design and Preparation of NLRP3-DZ. **a**: mouse sequence and binding state simulation results. **b**: human sequence and binding state simulation results. **c**: The cleaving activity of NLRP3-DZ was detected by gel electrophores(From left to right, is in the order of NLRP3-DZ,NLRP3-sub,NLRP3-DZ:NLRP3-sub = 1:1,NLRP3-DZ:NLRP3-sub = 1:5,NLRP3-DZ:NLRP3-sub = 1:10)

b: Pairing probability diagram of NLRP3-Dz and substrate chain binding process. c: schematic diagram of the action simulation of the human sequence.d: The cleaving activity of NLRP3-DZ was detected by gel electrophores.

Characterizations of NLRP3-DZ@ZIF-8/TAT hydrogels

ZIF-8 (zeolitic imidazolate framework-8), renowned for its unique properties such as a large surface area, high pore capacity, substantial loading potential, and remarkable stability under physiological conditions, serves as an attractive drug delivery system [29]. The SEM images in Fig. 3a reveal the polyhedral cubic crystal structure of NLRP3-DZ@ZIF-8/TAT, with particle sizes ranging from approximately 50 to 100 nm. Additionally, TEM analysis confirms the homogeneous dispersion of the hydrogels without observable agglomeration (Fig. 3e). In a similar study, ZIF-8 was decorated onto poly-chloropropyl-methyl-silsesquioxane to assess its loading capacity for acyclovir and tetracycline, further substantiating ZIF-8's ordered hollow pore structure [18].The results(Fig. 3d) show that the encapsulation rate of the material is about 71%, indicating that the ZIF-8@TAT encapsulation system is good and the effective utilization rate is high. The drug loading rate was about 9%, which may be related to the high quality of ZIF-8 containing metal ions.

The results of NLRP3-DZ@ZIF-8/TAT also exhibit a typical three-dimensional structure (Fig. 3h). The size analysis reveals that the size of ZIF-8 alone is approximately 40–50 nm, which aligns with the literature reports. The final polymer particle size is around 70–100 nm, indicating an increase in particle size and suggesting successful synthesis (Fig. 3b). Additionally, the zeta potential changed, with ZIF alone being positive by 10mV, while the final hydrogel form was about 20mV, which did not alter the charge properties of ZIF-8 (Fig. 3c). Comparable to the findings of this study, a dual pH/temperature-sensitive core-shell nanoformulation has been developed based on ZIF-8 [30].The resulting nanoparticles (NPs) exhibited particle sizes of approximately 200 nm and a zeta potential of about + 30mV. ZIF-8, a metal-organic framework, is formed through the coordination of zinc ions (Zn^{2+}) and 2-methylimidazole (2-MiM)., which exhibits good biocompatibility and sensitivity to acidic environments [31].The EDS (Fig. 3i) and XPS (Fig. 3j) patterns reveal the presence of C, N, O, P, and other basic elements that constitute NLRP3-DZ and

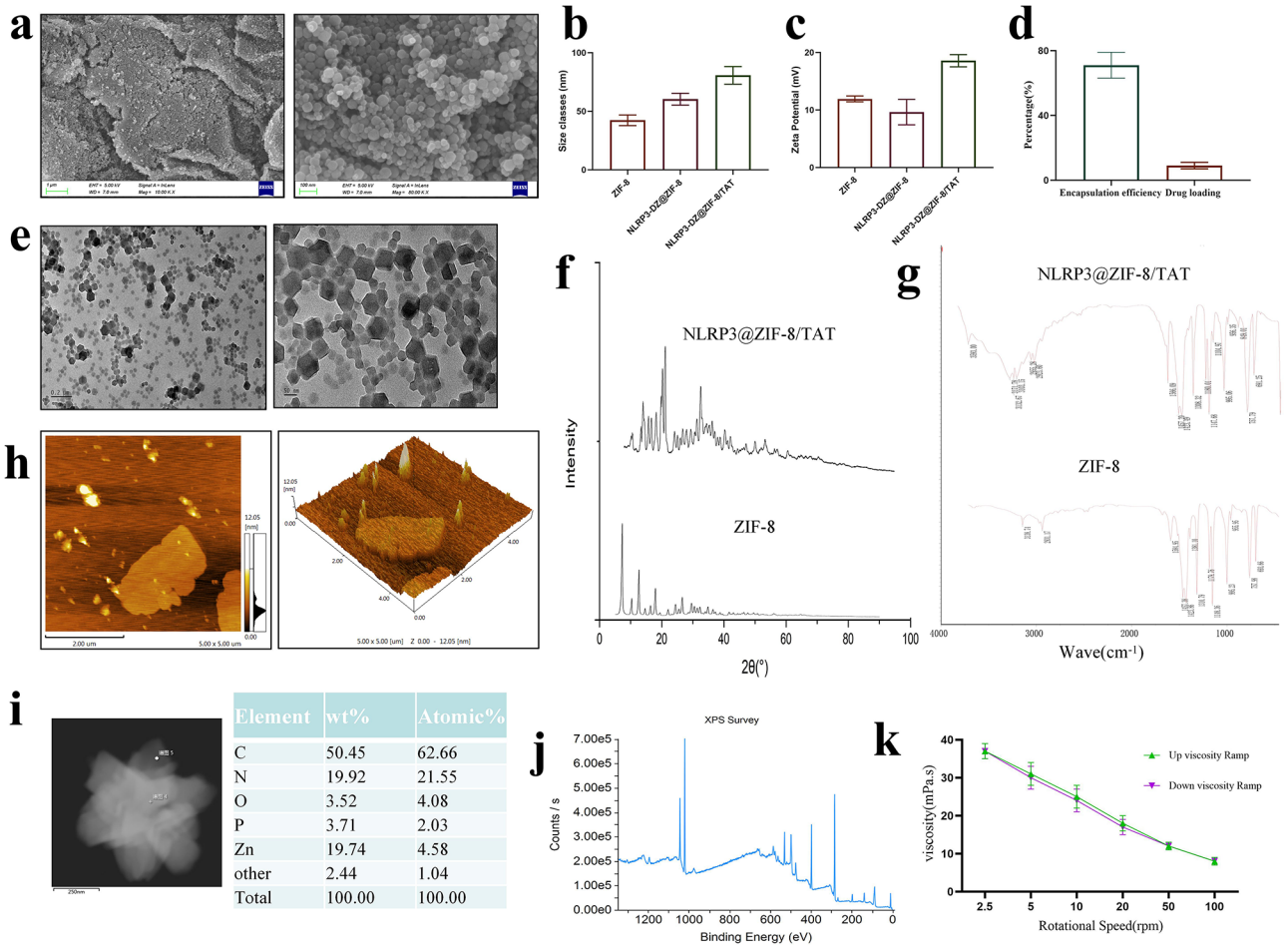

Fig. 3 Characterizations of NLRP3-DZ@ZIF-8/TAT Hydrogels. **a**: Material scanning electron microscope image (SEM); **b**: material particle size; **c**: Zeta charge of the material; **d**: Loading rate and encapsulation rate of the material; **e**: Material transmission electron microscope (TEM) image; **f**: X-ray diffraction pattern (XRD) of the material; **g**: Fourier infrared spectral image (FT-IR) of the material; **h**: Atomic force microscope image (AFM) of the material; **i**: Elemental Analysis Atlas of materials (EDS); **j**: X-ray photoelectron spectroscopy images (XPS) of the material; **k**: Viscosity image of NLRP3-DZ@ZIF-8/TAT

TAT, while the element Zn may originate from the purchased ZIF-8.

FTIR spectroscopy and XRD were utilized to gain insight into the interactions involved in loading NLRP3-DZ and TAT onto ZIF-8 (Fig. 3f and g). FTIR analysis was performed to determine the involvement of various functional entities present in the NLRP3-DZ@ZIF-8/TAT complex. Comparative spectra were illustrated for NLRP3-DZ@ZIF-8 and NLRP3-DZ@ZIF-8/TAT to distinguish the involvement of the functional groups present in the respective extracts [32]. The spectrum of ZIF-8 MOF exhibits absorption peaks at 757 and 691 cm^{-1}, attributed to the out-of-plane bending of the imidazole ring. The bending and stretching vibrations of the C-N bond in the 1,3-diazole ring are identified at 995 and 1147 cm^{-1}, respectively. Peaks at 1308 and 1423 cm^{-1} are assigned to the overall elongation of the imidazole ring, while the band at 1566 cm^{-1} is ascribed to the C = N stretching vibration. In the higher frequency region, the aliphatic and aromatic C–H stretches of 1,3-diazole are situated at 2923 and 3103 cm^{-1}, respectively. The band at 3132 cm^{-1} is endorsed by the vibrational stretching of the C-C bond in the imidazole ring. The broad band at around 3593 cm^{-1} is attributed to the O-H vibration in the bonded water. The FTIR spectra of the NLRP3-DZ@ZIF-8/TAT hybrid demonstrated absorption bands similar to those of pure MOF, with an additional band at 849 cm^{-1}, confirming successful encapsulation within the MOF cavities without structural alteration [33].The peak at 1381.10 cm^{-1} is attributed to the presence of the TAT peptide with NLRP3-DZ@ZIF-8, indicating a bathochromic shift. Shadmani et al. suggest that [34] the infrared spectrum showed an absorption band at 2033 cm^{-1}, indicative of successful TAT peptide functionalization. The stretching vibration of the amide I bond at 1627 cm^{-1} indicated successful grafting of the TAT peptide to MOF-NH2. For the spectrum of TAT-functionalized MSN, the increased peak intensity of N – H wagging and CH2

bending vibrations at 800 and 1390 cm^{-1}, respectively, was due to the presence of a large number of amine and methylene groups from the TAT group. Notably, The hydrogels were time-independent fluids, since the viscosity behavior did not change as a function of time when measuring at specific speeds: the down rate ramp matched the initial up rate ramp. The shear thinning behavior of the hydrogels is another important property. Hence, the hydrogels displayed a decrease of viscosity when the spindle rotational speed was increased(Fig. 3k). The XRD peaks align perfectly with previously reported data, confirming the assembly of a pure phase of ZIF-8 MOF [35]. It is worth noting that TAT in this study aims to enhance the transdermal properties of ZIF-8 [20], and there are also studies that use ZIF-8 as a drug carrier to enhance penetration.

The effect of NLRP3-DZ@ZIF-8/TAT for RISI cell models

Based on comprehensive literature reports, we speculate that NLRP3 overexpression plays a central role in the development of RISI [36, 37]. Therefore, designing DNAzyme (DZ)-hydrogels with targeted inhibition of NLRP3 overexpression is crucial for preventing RISI. HaCaT epidermal cells were co-cultured with NLRP3-DZ@ZIF-8/TAT for 7 days, and in Fig. 4a, the 3 Gy radiation in Group B affects the morphology of HaCaT cells, causing nuclear condensation and apoptotic morphology, while the use of NLRP3-DZ@ZIF-8/TAT in Group D can reverse this morphological change. CCK-8 assays showed that 3 Gy radiation inhibited the growth of HaCaT cells, while NLRP3-DZ@ZIF-8/TAT had no significant effect on the growth of HacAT cells (Fig. 4e). Xinrui et al. suggest that NLRP3 activation in epithelial cells after radiation, and initiates interleukin-1β secretion, affecting fibroblast activation, proliferation, and migration, leading to lung fibrosis [37]. Scratch tests on HaCaT cells co-cultured with materials from each group showed that group B's 24-hour mobility decreased significantly ($p < 0.05$), possibly due to radiation's effect on cell migration. Notably, migration inhibition was markedly reduced in group D (Fig. 4b + 4f). These findings indicate that NLRP3-DZ@ZIF-8/TAT promotes HaCaT cell migration post-radiation ($p < 0.05$).

The removal of invasive bacteria is crucial for proper RISI-wound healing. However, this task is challenging due to the intense oxidative stress triggered by these

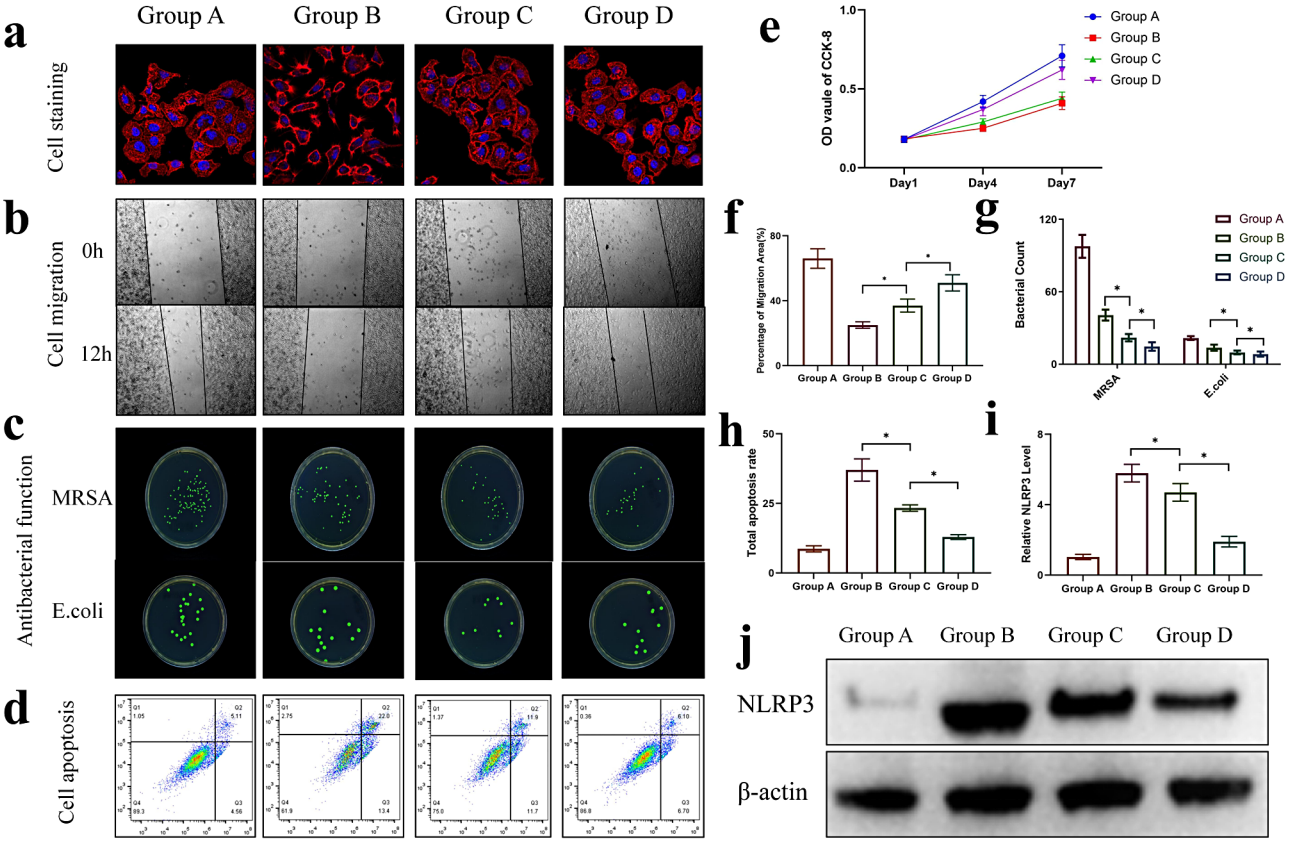

Fig. 4 The effects of NLRP3-DZ@ZIF-8/TAT on RISI cell models: **a**) FITC/DAPI staining of HaCaT cultures; **b** + **f**) Scratch wound migration assay for HaCaT cultures; **c** + **g**) Anti-bacterial activity against G+(MRSA) and G-(E.coli); **d** + **h**) Flow cytometry and apoptotic activity analysis; **e**) CCK-8 assay for HaCaT cultures on day 7; **j** + **i**) Western blotting for NLRP3 with semi-quantitative assessment. *$P < 0.05$, Normal cells(Group A), Normal cells + 3 Gy radiation(Group B), Normal cells + 3 Gy radiation + NLRP3-DZ(Group C), Normal cells + 3 Gy radiation + NLRP3-DZ@ZIF-8/TAT(Group D)

bacteria and their gradual development of antibiotic resistance. Antibacterial experiments (Fig. 4c + 4 g) demonstrated that NLRP3-DZ@ZIF-8/TAT had inhibitory effects on methicillin-resistant Staphylococcus aureus (MRSA, G+) and E. coli (G-). Mo et al.'s studies also discussed the anti-bacterial effect of DNAzyme material on wound surfaces [24].Here, we incorporated a DNAzyme into 2D NiCoCu metal-organic frameworks, which can adapt to infected wounds.Flow cytometry detection of the effect of NLRP3-DZ@ZIF-8/TAT on the apoptosis of HaCaT cells revealed that radiation increased the apoptosis rate (Fig. 4d + 4 h), while anti-NLRP3@ZIF-8 significantly decreased it ($p < 0.05$). Zhang's results revealed that [36] the number of NLRP3 inflammasomes increased in murine macrophage cell lines after irradiation (8 Gy), leading to decreased pyroptosis in macrophages. This mechanism may involve anti-NLRP3 inhibiting the expression of NLRP3.

By analyzing recent evidence [38], we identified NLRP3 inflammasome as a key mediator of radiation-induced injury, responding to radiation challenges, inducing cell pyroptosis and tissue dysfunction, and initiating non-resolving inflammation and fibrosis. Based on these findings, we propose early intervention/prevention strategies targeting the NLRP3 inflammasome in a radiation context, which may aid in resolving critical clinical problems. As shown in Fig. 4j + 4i, NLRP3-DZ@ZIF-8/TAT can effectively release NLRP3-DZ, thereby inhibiting the expression of NLRP3 mRNA and related proteins, and ultimately promoting cell migration and inhibiting cell apoptosis. In summary, in vitro cell models demonstrated that DZ-hydrogels have high biosafety, effectively inhibit the expression of NLRP3, promote cell migration, inhibit cell apoptosis, and possess antibacterial effects.

Effects of NLRP3-DZ@ZIF-8/TAT on HaCaT cell genomics induced by radiation

Recently, electron beams have been used to irradiate mice and rats in several studies [39, 40],Functional studies were performed using human keratinocytes (HaCaT) and skin fibroblasts (WS1). To investigate the potential use of NLRP3-DZ@ZIF-8/TAT therapy on human skin cells after radiation exposure, Affymetrix HTA2.0 expression profiling was used to identify differentially expressed genes (DEGs) in HaCaT cultures from Groups A, B, and D ($n = 3$), with the aim of identifying functional proteins or mRNA of interest. Figure 5a shows that compared to Group A, Group B had 275 upregulated genes and 342 downregulated genes, while Group D had 241 upregulated genes and 382 downregulated genes compared to Group B. Integrated analysis of metabolomics and transcriptomics revealed significant enrichment and increase in six key fatty acid-associated metabolites, nine key fatty acid-associated genes, and multiple fatty acid-associated pathways in irradiated skin [39].This study indicates that cutaneous fatty acid metabolism is altered in the early response to ionizing radiation, and fatty acid metabolism-associated ACADVL is involved in radiation-induced cell death (Fig. 5b and c).Thomas et al. described a radiation-induced model we developed using zebrafish [41],where transcriptomic and behavioral analyses were conducted, revealing radiation-induced perturbations in lipid metabolism and absorption, wound healing, immune response, and fibrogenic pathways. Principal Components Analysis (Fig. 5d) and Gene expression distribution (Fig. 5e) further confirmed the significant changes in mRNA composition in response to NLRP3-DZ@ZIF-8/TAT. Similarly, Peng's study [42] demonstrated that Retinyl palmitate possesses significant anti-photoaging properties, metabolomics and transcriptomics results suggest that Retinyl palmitate regulates multiple metabolic pathways and gene expression, particularly in inflammatory signaling pathways, collagen synthesis, and apoptosis, exhibiting notable regulatory effects.

The Gene Ontology (GO) is a comprehensive database describing gene functions, categorized into biological process, cellular component, and molecular function. GO assessment indicated that radiation exposure upregulated multiple genes associated with inflammatory response, oxidative stress, regulation of cytokine production, and protein-binding function (Fig. 5f). This is consistent with our previous research. A biomaterial was designed for healing radio-induced injuries using multiple strategies [43].Genomics assessment showed it could improve abnormal skin culture expression due to radiation. A murine model indicated biomaterial reduced ROS and NLRP3 expression while promoting wound recovery. The KEGG database was used to determine vital pathways of differentially expressed genes. As shown in Fig. 5g, the top upregulated pathways included cytokine-cytokine receptor interactions, antivirus-related pathways, the IL-17 signaling pathway, and the HIF-1 signaling pathway, indicating involvement in inflammatory and oxidative stress responses. Su et al.'s study aimed to identify dasatinib's targets and signaling pathways in treating radiation ulcers using network pharmacology and molecular docking technology [44].Finally, the identified core targets were subjected to GO and KEGG enrichment analysis. Core targets were analyzed using GO and KEGG. Dasatinib may treat radiation ulcers by regulating EGFR, ERBB2, FYN, JAK2, KIT, and SRC. GO analysis showed senescent fibroblasts are involved in immune effector processes, and KEGG analysis identified the IL-17 signaling pathway, cytokine-cytokine receptor interaction, and xenobiotic metabolism as main pathways [45]. Genomics has shown that DZ-hydrogels may perform these functions by regulating changes in relevant mRNA pathways.

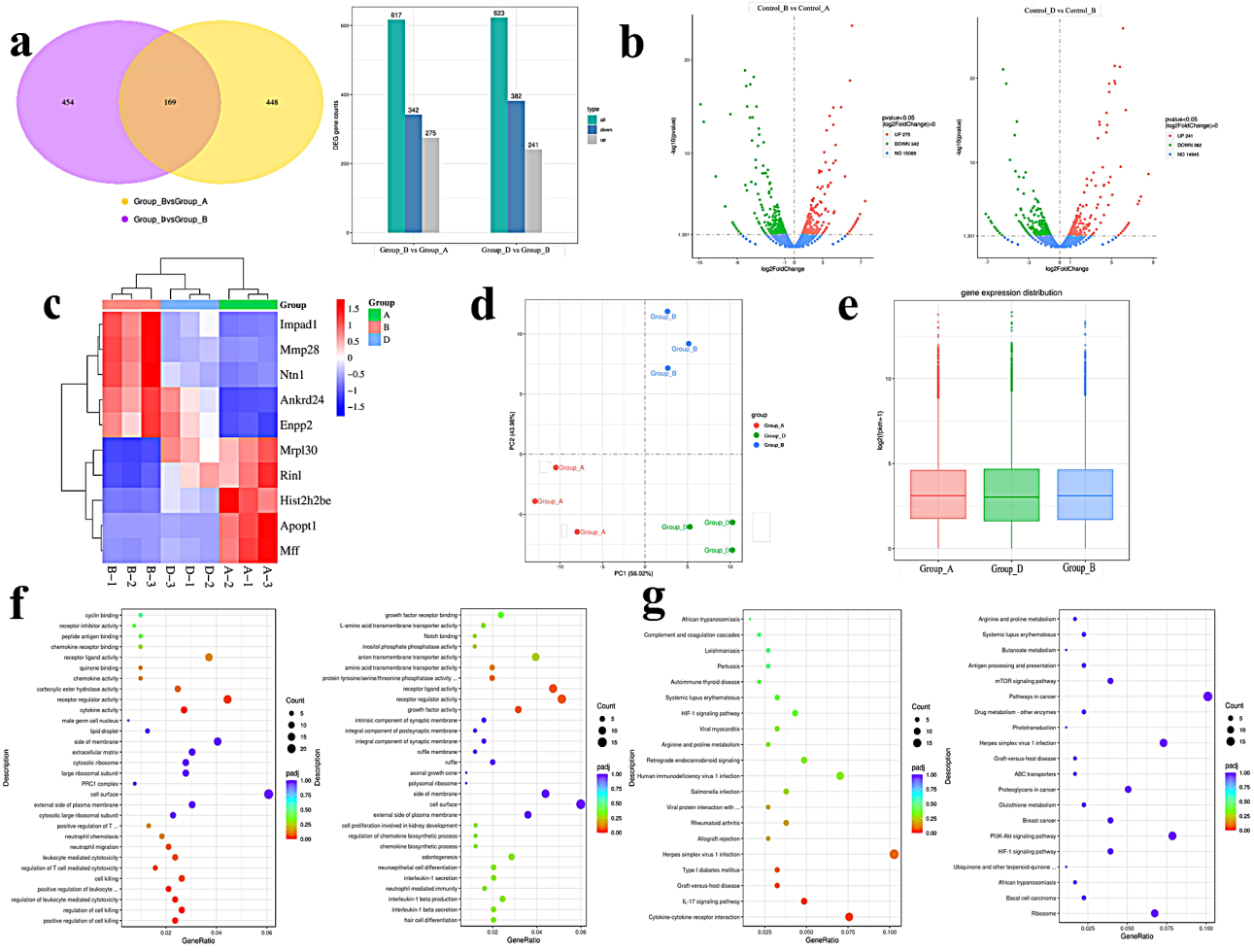

Fig. 5 Effects of NLRP3-DZ@ZIF-8/TAT on HaCaT cell genomics induced by radiation. **a**: The DEG gene counts.b: Volcano map of differentially expressed genes. **c**: Differential expression gene clustering. **d**: Principal Components Analysis. **e**: gene expression distribution. **f**: GO biological process and GO molecular function assessment. **g**: KEGG pathway assessment for DEGs.Normal cells(Group A), Normal cells + 3 Gy radiation(Group B), Normal cells + 3 Gy radiation + NLRP3-DZ@ZIF-8/TAT(Group D).Picture (left): Group B VS Group A, picture(right): Group D VS Group B, $n = 3$

The effect of NLRP3-DZ@ZIF-8/TAT for RISI mice model and mechanisms

Five different groups, referred to as Groups A-E, were used for the mice-RISI experiments. These groups consisted of normal mice, normal mice + 30 Gy radiation, normal mice + 30 Gy radiation + NLRP3-DZ, normal mice + 30 Gy radiation + NLRP3-DZ@ZIF-8, and normal mice + 30 Gy radiation + NLRP3-DZ@ZIF-8/TAT, respectively. As shown in Fig. 6a, all mice were depilated on Day 1 and then irradiated with 30 Gy to compare the effects of different intermediate and end products. The mice were euthanized on the 14th day after irradiation, and their wound morphology and related indices were compared. From a general morphological perspective, radiation of 30 Gy alone (Group B) caused mice to develop RISI of Grade 3–4, with a large wound area and inhibited hair follicle growth. The final material group, Group E, effectively inhibited RISI, with better results than the intermediate material groups, C and D. Our previous study also designed a paintable graphene oxide-hybridized soy protein-based biogel for skin radioprotection, and similar results were predicted for wound surfaces in mice [43]. This indicates that functional biomaterials can effectively ameliorate radiation-induced wound damage. The relative wound area and complete healing time also conformed to this pattern (Fig. 6b and c). The relative wound area caused by radiation (Group B) was the largest, while Group E effectively reduced the size of the wound area and shortened the complete healing time. At the same time, the weight of the mice was closely related to the severity of radiation damage. As can be seen from Fig. 6d, Group E could restore the normal weight of mice as soon as possible by reducing radiation damage, which also confirms the effectiveness of the material. We observed similar results in another study where We designed multifunctional mesoporous silica-cerium oxide nanozymes to facilitate miR129 delivery, aiming for high-quality healing of radiation-induced skin injury

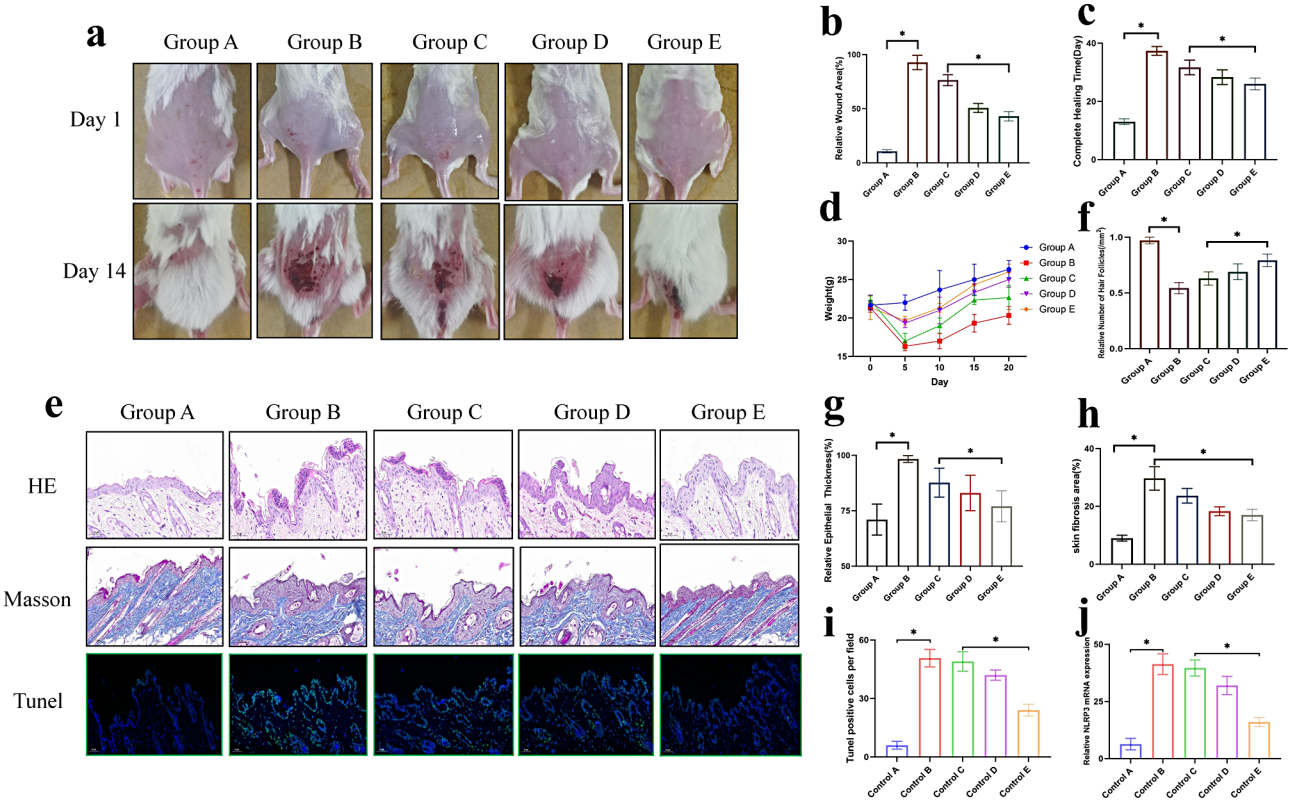

Fig. 6 The effect of NLRP3-DZ@ZIF-8/TAT for RISI mice model. **a**:The skin of mice irradiated on day 1 and day 14 was compared. **b**:Comparison of the relative wound area in mice 14 days after irradiation. **c**:Comparison of wound healing time after irradiation in mice. **d**:Weight change of mice after irradiation. **e**:HE, Masson and Tunnel stain upon day14. f: Comparison of the number of hair follicles in the wound of mice. **g**:Changes of relative epithelial thickness in mice after irradiation.h: Comparison of Masson staining on the skin fibrosis area(%). **i**:Quantitative analysis of Tunnel staining. **j**:Quantitative analysis of NLRP3 mRNA.Normal mice(Group A), Normal mice + 30 Gy(Group B), Normal mice + 30 Gy radiation + NLRP3-DZ(Group C), Normal mice + 30 Gy + NLRP3-DZ@ZIF-8(Group D), Normal mice + 30 Gy + NLRP3-DZ@ZIF-8/TAT(Group E), **P* < 0.05

[46]. It was found that the composite material effectively reduced the size of the wound area and shortened the complete healing time.

Assessment of the H&E staining dataset outcomes demonstrated that radiation can significantly decrease the growth of wound hair follicles and increase the relative epithelial thickness (Fig. 6e and f, and 6g). Regarding H&E staining results, we have designed an IFI6-based hydrogel that promotes the healing of radiation-induced skin injury through regulation of HSF1 activity, and this biomaterial was also found to promote hair follicle density and relative epithelial thickness [7].Additionally, another study on injectable miR181a-IFI6 nanoparticles promotes high-quality healing of radiation-induced skin injury, demonstrating a similar phenomenon [8].These dataset outcomes suggest that NLRP3-DZ@ZIF-8/TAT enhances migrative and proliferative activity for epidermal cells, reduces the rate of apoptosis, thereby inducing wound recovery.

Masson's trichrome staining showed that collagen fibers appeared blue, while muscle fibers, cytoplasm, cellulose, keratin, and erythrocytes were stained red, and nuclei exhibited a blue-brown color [47].Collagen ratios impact the tensile strength of the wound, increasing from 20% to a maximum of 70% of normal skin three weeks after the injury. Therefore, collagen is able to interact with various regenerative pathways in skin wound healing. As shown in Fig. 6e and h, radiation can increase collagen fibers in skin epithelial tissue and initiate the repair process, while group E can further improve the condition of collagen fibers and ultimately repair the wound epithelium. Xiang et al. propose that UVB irradiation in vivo induces hyperkeratosis, dermis destruction, decreased collagen fibers, elevated cellular senescence, and oxidative stress activation in hairless mice [48]. Laser treatment, on the other hand, thins the stratum corneum of skin tissue, enhances collagen synthesis and autophagy in the dermis, and reduces oxidative stress levels.It is worth noting that, as far as animal experiments are concerned, the improvement effect of each group on RISI generally follows the order: NLRP3-DZ@ZIF-8/TAT > NLRP3-DZ@ZIF-8 > NLRP3-DZ. As mentioned in the preface, this demonstrates two points: the use of ZIF-8 encapsulation to enhance the stability, controlled release, and

safety of NLRP3-DZ [17, 18]; and the enhancement of material transdermal quantity and practicality by attaching the TAT transmembrane peptide [20, 34].

Finally, we evaluated the impact of the materials on inflammatory response and oxidative stress mechanisms in RISI mice. As depicted in Fig. 4d, the apoptosis study revealed that NLRP3-DZ effectively reduces the apoptosis rate. To further validate this finding, we utilized the mouse RISI model. As illustrated in Fig. 6e + 6i, Under ultraviolet excitation, the nuclei stained with DAPI appeared blue, whereas the kit, labeled with FITC fluorescein, indicated positive apoptotic nuclei in green. Notably, the Tunel staining positive rate was highest in Group B, suggesting that radiation energy increased the apoptosis rate of mouse skin. Conversely, the DZ material in Group E (NLRP3-DZ@ZIF-8/TAT) significantly reduced the apoptosis rate. Tunel staining has long been employed to assess skin apoptosis, with studies on wound healing analyzed both qualitatively and quantitatively using this method [49].Overall, the materials demonstrated excellent biocompatibility, promoting cell activity without any indications of increased apoptosis.

Based on recent evidence [38], Cheng et al. identified the NLRP3 inflammasome as a crucial executor of radiation-induced injury, responding to radiation challenges, inducing cell pyroptosis and tissue dysfunction, and initiating non-resolving inflammation and fibrosis. In Fig. 4j, we assessed NLRP3 expression at the skin cell level and found that NLRP3-DZ effectively inhibited NLRP3 protein expression. To further validate this, we conducted tests on RISI mice (Fig. 6j). Similarly, radiation significantly increased NLRP3 expression in Group B, mediating the inflammatory response. Group E, however, effectively reduced NLRP3 mRNA expression in mouse skin, although the inhibitory effect was less pronounced than at the cellular level, it still demonstrated a favorable outcome. Rao et al. suggest that NLRP3 inflammasome activation in lung epithelial cells is crucial for radiation-induced lung injury [37]. Furthermore, Zhang et al.'s findings implicate the miR-223-3p/NLRP3/caspase-1 axis in radiation-induced alveolar macrophage (AM) pyroptosis and lung injury [36].These data strongly indicate that targeting NLRP3 may be effective in mitigating radiation-induced injury in clinical settings.

In summary, these mechanistic studies demonstrate that NLRP3-DZ@ZIF-8/TAT can inhibit oxidative stress and inflammatory response, ultimately facilitating wound healing in RISI mice by regulating NLRP3.

Conclusion

The study aims to enhance the stability, controlled release, and safety of NLRP3-DZ by utilizing ZIF-8 encapsulation. The TAT transmembrane peptide is attached to enhance the material's transdermal quantity and practicality. The final preparation and characterization of NLRP3-DZ@ZIF-8/TAT were carried out. In vitro cell models demonstrated that DZ-hydrogels exhibit high biosafety, effectively inhibit NLRP3 expression, promote cell migration, inhibit cell apoptosis, and possess antibacterial effects. Genomics analysis revealed that DZ-hydrogels may exert these functions by regulating changes in relevant mRNA pathways. Lastly, a mice RISI model was proposed, and it was found that the material can promote wound healing by regulating proteins related to apoptosis, oxidative stress, and inflammatory response. The research results provide a valuable reference for the prevention of RISI using DZ-hydrogels.Meanwhile, in the later stages, we will endeavor to actively carry out Phase I clinical research work on the basis of further refining and improving the relevant research.

Acknowledgements
We thank Shiyanjia Lab (https://www.shiyanjia.com) and Nanjing XFNANO for its technical support. We thank M.E. Fornace et al (https://doi.org/10.26434/chemrxiv-2022-xv98l) for its software support.

Author contributions
Daijun Zhou: Design and Experiment. Zhihui Li and Linbo Bao: Cell experiments.Xiang Zhao and Jie Hao: Animal experiments.Chuan Xu and Feifan Sun: Material design and characterization. Dan He: Conceptualization and Methodology.Chaoyang Jiang and Tian Zeng: Writing - review & editing, Supervision. Dong Li: Project administration.

Funding
This study was supported by The Youth Program of Sichuan Natural Science Foundation (2023NSFSC1841), The Program of General Hospital of Western Theater Command (2024-YGJC-A11/2024-YGJS-A04), the School level Program of Army Medical University (2022XQN26), the Scientific Research Project of China Baoyuan(CBYI202103).

Data availability
No datasets were generated or analysed during the current study.

Declarations

Ethics approval and consent
The experimental design, process, and animal killing methods were reviewed and approved by the Laboratory Animal Welfare and Ethics Committee of Southwest Hospital, meeting animal ethics and welfare requirements.

Consent for publication
Not applicable.

Competing interests
The authors declare no competing interests.

Received: 22 July 2024 / Accepted: 22 January 2025
Published online: 22 March 2025

References

1. Malekzadeh H, Surucu Y, Chinnapaka S, et al. Metformin and adipose-derived stem cell combination therapy alleviates radiation-induced skin fibrosis in mice[J]. Stem Cell Res Ther. 2024;15(1). https://doi.org/10.1186/s13287-023-03627-7.
2. Wei KC, Lai SF, Huang WL, et al. An innovative targeted therapy for fluoroscopy-induced chronic radiation dermatitis[J]. J Mol Med (Berl). 2022;100(1):135–46. https://doi.org/10.1007/s00109-021-02146-3.

3. Rzepecki A, Birnbaum M, Ohri N, et al. Characterizing the effects of radiation dermatitis on quality of life: a prospective survey-based study[J]. J Am Acad Dermatol. 2022;86(1):161–3. https://doi.org/10.1016/j.jaad.2019.03.011.
4. Gojsevic M, Kennedy S, Rajeswaran T, et al. Patient-reported experience with the use of Mepitel Film for prevention of acute radiation dermatitis in breast cancer[J]. Support Care Cancer. 2024;32(1). https://doi.org/10.1007/s00520-023-08302-4.
5. Zetner D, Kamby C, Gulen S, et al. Quality-of-life outcomes following topical melatonin application against acute radiation dermatitis in patients with early breast cancer: a double-blind, randomized, placebo-controlled trial[J]. J Pineal Res. 2023;74(1):e12840. https://doi.org/10.1111/jpi.12840.
6. Ma Z, Chen Y, Tang K, et al. Highly efficient prevention of radiation dermatitis using a PEGylated superoxide dismutase dissolving microneedle patch[J]. Eur J Pharm Biopharm. 2024;201:114347. https://doi.org/10.1016/j.ejpb.2024.114347.
7. Hao J, Sun M, Li D, et al. An IFI6-based hydrogel promotes the healing of radiation-induced skin injury through regulation of the HSF1 activity[J]. J Nanobiotechnol. 2022;20(1). https://doi.org/10.1186/s12951-022-01466-x.
8. Zhou D, Hao J, Li D, et al. An injectable miR181a-IFI6 nanoparticles promote high-quality healing of radiation-induced skin injury[J]. Mater Today Adv. 2022;15:100267DOI. https://doi.org/10.1016/j.mtadv.2022.100267.
9. Huang R, Sun W, Li W, et al. Immunomodulatory hydrogel patches loaded with curcumin and tannic acid assembled nanoparticles for radiation dermatitis repair and radioprotection[J]. Chem Eng J. 2024;500:156869DOI. https://doi.org/10.1016/j.cej.2024.156869.
10. Lee H, Huang Y, Huang J, et al. Exploring black soybean extract cream for inflammatory dermatitis—toward Radiation Dermatitis Relief[J]. Int J Mol Sci. 2024;25(21):11598. https://doi.org/10.3390/ijms252111598.
11. Finkelstein S, Kanee L, Behroozian T, et al. Comparison of clinical practice guidelines on radiation dermatitis: a narrative review[J]. Support Care Cancer. 2022. https://doi.org/10.1007/s00520-022-06829-6.
12. Lee CJ, Fang HF, Wang CY, et al. Effect of hyaluronic acid on radiodermatitis in patients with breast cancer: a meta-analysis of randomized controlled trials[J]. Support Care Cancer. 2022. https://doi.org/10.1007/s00520-022-06828-7.
13. Finkelstein S, Kanee L, Behroozian T, et al. Comparison of clinical practice guidelines on radiation dermatitis: a narrative review[J]. Support Care Cancer. 2022;30(6):4663–74. https://doi.org/10.1007/s00520-022-06829-6.
14. Lansink Rotgerink L, Felchle H, Feuchtinger A, et al. Experimental investigation of skin toxicity after immune checkpoint inhibition in combination with radiation therapy[J]. J Pathol. 2022. https://doi.org/10.1002/path.5989.
15. Wu S, Zhang K, Liang Y, et al. Nano-enabled Tumor systematic energy exhaustion via zinc (II) interference mediated glycolysis inhibition and specific GLUT1 Depletion[J]. Adv Sci (Weinh). 2022;9(7):e2103534. https://doi.org/10.1002/advs.202103534.
16. Ma Y, Duan X, Huang J. DNA hydrogels as functional materials and their Biomedical Applications[J]. Adv Funct Mater. 2024;34(3). https://doi.org/10.1002/adfm.202309070.
17. Zhu J, Wen T, Qu S, et al. G-Quadruplex/Hemin DNAzyme-Functionalized silver nanoclusters with synergistic Antibacterial and Wound Healing capabilities for infected Wound Management[J]. Small. 2024;20(8):e2307220. https://doi.org/10.1002/smll.202307220.
18. Teimouri M, Mirzaee M, Nemati A, et al. Polysilsesquioxane decorated ZIF-8 as a potential pH-responsive vehicle for topical delivery and release of acyclovir and tetracycline: investigation of blood compatibility, cytotoxicity and antibacterial properties[J]. Int J Biol Macromol. 2024;271(Pt 1):132542DOI. https://doi.org/10.1016/j.ijbiomac.2024.132542.
19. Zhang S, Yi J, Yuan X, et al. Fabrication and characterization of carrageenan-based multifunctional films integrated with gallic acid@ZIF-8 for beef preservation[J]. Int J Biol Macromol. 2024;274(Pt 1):133319DOI. https://doi.org/10.1016/j.ijbiomac.2024.133319.
20. Mi Z, Ma J, Zeh DJ, et al. Systemic treatment with ubiquitin carboxy terminal hydrolase L1 TAT protein ameliorates axonal injury and reduces functional deficits after traumatic brain injury in mice[J]. Exp Neurol. 2024;373:114650DOI. https://doi.org/10.1016/j.expneurol.2023.114650.
21. Zhu Z, Zhai Y, Hao Y, et al. Specific anti-glioma targeted-delivery strategy of engineered small extracellular vesicles dual-functionalised by Angiopep-2 and TAT peptides[J]. J Extracell Vesicles. 2022;11(8). https://doi.org/10.1002/jev2.12255.
22. Zhang Y, Fang M, Li S, et al. BTApep-TAT peptide inhibits ADP-ribosylation of BORIS to induce DNA damage in cancer[J]. Mol Cancer. 2022;21(1). https://doi.org/10.1186/s12943-022-01621-w.
23. Zhu J, Wen T, Qu S, et al. G-Quadruplex/Hemin DNAzyme-Functionalized Silver Nanoclusters with Synergistic Antibacterial and Wound Healing capabilities for infected Wound Management[J]. Small. 2024;20(8). https://doi.org/10.1002/smll.202307220.
24. Mo F, Lin C, Lu J, et al. Integrating Artificial DNAzymes with natural enzymes on 2D MOF hybrid nanozymes for enhanced treatment of Bacteria-infected Wounds[J]. Small. 2024;20(21):e2307256. https://doi.org/10.1002/smll.202307256.
25. Borggräfe J, Victor J, Rosenbach H, et al. Time-resolved structural analysis of an RNA-cleaving DNA catalyst[J]. Nat (London). 2022;601(7891):144–9. https://doi.org/10.1038/s41586-021-04225-4.
26. Yan J, Ran M, Shen X, et al. Therapeutic DNAzymes: from structure design to clinical Applications[J]. Adv Mater. 2023;35(30):e2300374. https://doi.org/10.1002/adma.202300374.
27. Miao Q, Ding W, Bao X, et al. An efficient DNAzyme for the fluorescence detection of Vibrio cholerae[J]. Food Sci Nutr. 2023;11(6):3235–45. https://doi.org/10.1002/fsn3.3304.
28. Zhang Y, Wu L, Su X, et al. Construction of a highly efficient DNA nanotube sensor with peroxide-like activity[J]. J Mater Chem B. 2023;12(1):240–9. https://doi.org/10.1039/d3tb01984e.
29. Oryani MA, Nosrati S, Javid H, et al. Targeted cancer treatment using folate-conjugated sponge-like ZIF-8 nanoparticles: a review[J]. Naunyn Schmiedebergs Arch Pharmacol. 2024;397(3):1377–404. https://doi.org/10.1007/s00210-023-02707-y.
30. Dashti N, Akbari V, Varshosaz J, et al. Co-delivery of carboplatin and doxorubicin using ZIF-8 coated chitosan-poly(N-isopropyl acrylamide) nanoparticles through a dual pH/thermo responsive strategy to breast cancer cells[J]. Int J Biol Macromol. 2024;269(Pt 1):131971DOI. https://doi.org/10.1016/j.ijbiomac.2024.131971.
31. Guo B, Sun Y, Guan Q, et al. Fabrication and characterization of sodium alginate/blueberry anthocyanins/hinokitiol loaded ZIF-8 nanoparticles composite films with antibacterial activity for monitoring pork freshness[J]. Food Chem. 2024;440:138200. https://doi.org/10.1016/j.foodchem.2023.138200.
32. Majeed S, Saravanan M, Danish M, et al. Bioengineering of green-synthesized TAT peptide-functionalized silver nanoparticles for apoptotic cell-death mediated therapy of breast adenocarcinoma[J]. Talanta. 2023;253:124026DOI. https://doi.org/10.1016/j.talanta.2022.124026.
33. Du T, Shi Z, Mou X, et al. Axial assembly of AuNR for tumor theranostics via Zn(2+)-GSH chelation induced degradation of AuNR@ZIF-8 heterostructures[J]. Colloids Surf B Biointerfaces. 2024;234:113706. https://doi.org/10.1016/j.colsurfb.2023.113706.
34. Shadmani N, Makvandi P, Parsa M, et al. Enhancing Methotrexate Delivery in the brain by mesoporous silica nanoparticles functionalized with cell-penetrating peptide using in Vivo and ex vivo Monitoring[J]. Mol Pharm. 2023;20(3):1531–48. https://doi.org/10.1021/acs.molpharmaceut.2c00755.
35. Abdelkhalek MM, Mohamed AM, Abdallah RZ, et al. Zeolitic imidazolate framework-8 encapsulated with Mo-based polyoxometalates as surfaces with antibacterial activity against Escherichia coli[J]. Nanoscale Adv. 2024;6(13):3355–66. https://doi.org/10.1039/d4na00142g.
36. Zhang M, Lan H, Peng S, et al. MiR-223-3p attenuates radiation-induced inflammatory response and inhibits the activation of NLRP3 inflammasome in macrophages[J]. Int Immunopharmacol. 2023;122:110616DOI. https://doi.org/10.1016/j.intimp.2023.110616.
37. Rao X, Zhou D, Deng H, et al. Activation of NLRP3 inflammasome in lung epithelial cells triggers radiation-induced lung injury[J]. Respir Res. 2023;24(1):25. https://doi.org/10.1186/s12931-023-02331-7.
38. Cheng H, Chen L, Huang M, et al. Hunting down NLRP3 inflammasome: an executioner of radiation-induced injury[J]. Front Immunol. 2022;13:967989. https://doi.org/10.3389/fimmu.2022.967989.
39. Tu W, Tang S, Yan T, et al. Integrative multi-omic analysis of radiation-induced skin injury reveals the alteration of fatty acid metabolism in early response of ionizing radiation[J]. J Dermatol Sci. 2022;108(3):178–86. https://doi.org/10.1016/j.jdermsci.2023.01.001.
40. Griffin GK, Booth C, Togami K, et al. Ultraviolet radiation shapes dendritic cell leukaemia transformation in the skin[J]. Nature. 2023;618(7966):834–41. https://doi.org/10.1038/s41586-023-06156-8.
41. Cahill T, Da SW, Renaud L, et al. Investigating the effects of chronic low-dose radiation exposure in the liver of a hypothermic zebrafish model[J]. Sci Rep. 2023;13(1):918. https://doi.org/10.1038/s41598-022-26976-4.
42. Shu P, Li M, Zhao N, et al. Efficacy and mechanism of retinyl palmitate against UVB-induced skin photoaging[J]. Front Pharmacol. 2023;14:1278838. https://doi.org/10.3389/fphar.2023.1278838.

43. Zhou D, Liu H, Han L, et al. Paintable graphene oxide-hybridized soy protein-based biogels for skin radioprotection[J]. Chem Eng J. 2023;469. https://doi.org/10.1016/j.cej.2023.143914.
44. Su W, Chen X, Zhang W, et al. Therapeutic targets and signaling mechanisms of dasatinib activity against radiation skin ulcer[J]. Front Public Health. 2022;10:1031038. https://doi.org/10.3389/fpubh.2022.1031038.
45. Qiang M, Dai Z. Biomarkers of UVB radiation-related senescent fibroblasts[J]. Sci Rep. 2024;14(1):933. https://doi.org/10.1038/s41598-023-51058-4.
46. Zhou D, Du M, Luo H, et al. Multifunctional mesoporous silica-cerium oxide nanozymes facilitate miR129 delivery for high-quality healing of radiation-induced skin injury[J]. J Nanobiotechnol. 2022;20(1). https://doi.org/10.1186/s12951-022-01620-5.
47. Gardeazabal L, Izeta A. Elastin and collagen fibres in cutaneous wound healing[J]. Exp Dermatol. 2024;33(3):e15052. https://doi.org/10.1111/exd.15052.
48. Xiang H, Jia X, Duan X, et al. Q-switched 1064 nm nd: YAG laser restores skin photoageing by activating autophagy by TGFbeta1 and ITGB1[J]. Exp Dermatol. 2024;33(1):e15006. https://doi.org/10.1111/exd.15006.
49. Strenge JT, Smeets R, Nemati F, et al. Biodegradable Silk Fibroin matrices for Wound Closure in a human 3D Ex vivo Approach[J]. Mater (Basel). 2024;17(12). https://doi.org/10.3390/ma17123004.

Publisher's note